Measurement of the polarisation of W bosons produced in top-quark decays using dilepton events at $\sqrt{s}$ = 13 TeV with the ATLAS experiment

The ATLAS Collaboration

A measurement of the polarisation of W bosons produced in top-quark decays is presented, using proton–proton collision data at a centre-of-mass energy of $\sqrt{s}$ = 13 TeV. The data were collected by the ATLAS detector at the Large Hadron Collider and correspond to an integrated luminosity of 139 fb^{-1}. The measurement is performed selecting $t\bar{t}$ events decaying into final states with two charged leptons (electrons or muons) and at least two b-tagged jets. The polarisation is extracted from the differential cross-section distribution of the $\cos\theta^*$ variable, where θ^* is the angle between the momentum direction of the charged lepton from the W boson decay and the reversed momentum direction of the b-quark from the top-quark decay, both calculated in the W boson rest frame. Parton-level results, corrected for the detector acceptance and resolution, are presented for the $\cos\theta^*$ angle. The measured fractions of longitudinal, left- and right-handed polarisation states are found to be $f_0 = 0.684 \pm 0.005\,(\text{stat.}) \pm 0.014\,(\text{syst.})$, $f_L = 0.318 \pm 0.003\,(\text{stat.}) \pm 0.008\,(\text{syst.})$ and $f_R = -0.002 \pm 0.002\,(\text{stat.}) \pm 0.014\,(\text{syst.})$, in agreement with the Standard Model prediction.

1 Introduction

Discovered in 1995 by the CDF and D0 experiments [1, 2], the top quark is the heaviest known elementary particle so far. Its abundant production at the Large Hadron Collider (LHC) allows its properties to be measured with unprecedented precision. The properties of the top-quark decay vertex Wtb are determined by the $(V - A)$ structure of the weak interaction in the Standard Model (SM), where V and A refer to the vector and axial-vector components of the weak interaction, respectively. The Wtb vertex structure, and the masses of the three particles, govern the decay properties of the W boson produced in the top-quark decay. In particular, they define the fractions of longitudinal (f_0), left-handed (f_L) and right-handed (f_R) polarised W bosons, referred to as helicity fractions. Calculations at next-to-next-to-leading order (NNLO) in quantum chromodynamics (QCD) yield the following values for the fractions: $f_0 = 0.687 \pm 0.005$, $f_L = 0.311 \pm 0.005$ and $f_R = 0.0017 \pm 0.0001$ assuming a top-quark mass $m_{\text{top}} = 172.8$ GeV, a W boson mass $m_W = 80.401$ GeV and a b-quark mass $m_b = 4.8$ GeV [3]. The uncertainties in the f_0 and f_L fractions are dominated by the experimental uncertainties in the top-quark mass, while the uncertainty in f_R is dominated by uncertainties in the strong coupling constant and the b-quark mass. This analysis tests the structure of the Wtb vertex by measuring the helicity fractions of W bosons produced in top-quark decays with high precision. Precise measurements of these fractions can probe possible new physics processes which modify the structure of the Wtb vertex, such as dimension-six operators, introduced in effective field theories [4, 5]. The helicity fractions f_0 and f_L are especially sensitive to the C_{tW} Wilson coefficient [6], and at the level of squared dimension-6 operators, C_{bW} and $C_{\phi tb}$ also affect them. Additionally, the expected value of f_R is very small, making it particularly sensitive to possible signs of new physics. The $W\ell\nu$ vertex is assumed to follow the SM prediction, in accord with extensive studies of this vertex at LEP [7–11].

The W boson helicity fractions can be extracted from measurements of the angular distribution of the decay products of the W boson and the top quark. The eight-component W boson spin density matrix, with three spin-operator and five tensor-operator components, entirely determines the angular distribution of the products of the leptonic decay $W^\pm \to \ell^\pm \nu$, with $\ell = e, \mu, \tau$. It can be expressed in terms of the polar and azimuthal angles of the charged-lepton momentum in the W boson rest frame. Integrating over the azimuthal angle, the off-diagonal contributions vanish, and the normalised differential distribution of the cosine of the polar angle θ^*, $\cos \theta^*$, depends on the helicity fractions as [12]

$$\frac{1}{\sigma} \frac{d\sigma}{d\cos\theta^*} = \frac{3}{4}(1 - \cos^2\theta^*)f_0 + \frac{3}{8}(1 - \cos\theta^*)^2 f_L + \frac{3}{8}(1 + \cos\theta^*)^2 f_R. \tag{1}$$

The angle θ^* is defined as the angle between the momentum direction of the charged lepton from the W boson decay and the reversed momentum direction of the b-quark from the decay of the top quark, both calculated in the W boson rest frame.

Previous measurements of the W boson helicity fractions from the ATLAS [13], CMS [14], CDF [15], and D0 [16, 17] collaborations are in agreement with the SM predictions within their uncertainties. The most recent ATLAS measurement was performed in the single-lepton channel of $t\bar{t}$ decays at 8 TeV [13] and obtained $f_0 = 0.709 \pm 0.012 \,(\text{stat.} + \text{bkg.}) \, ^{+0.015}_{-0.014} \,(\text{syst.})$, $f_L = 0.299 \pm 0.008 \,(\text{stat.} + \text{bkg.}) \, ^{+0.013}_{-0.012} \,(\text{syst.})$ and $f_R = -0.008 \pm 0.006 \,(\text{stat.} + \text{bkg.}) \pm 0.012 \,(\text{syst.})$ using the template fit method. This result was combined with measurements from CMS to yield the combined result $f_0 = 0.693 \pm 0.014$, $f_L = 0.315 \pm 0.011$ and $f_R = -0.008 \pm 0.007$, where total uncertainties are quoted [18].

This Letter presents a measurement of the W helicity fractions in the dileptonic final state of the $t\bar{t}$ pair. Electron and muon final states are probed, including the leptonic decays of τ-leptons. This decay mode is chosen for its very small background contamination. The measurement uses the full set of ATLAS pp collision data at $\sqrt{s}$ = 13 TeV, which corresponds to an integrated luminosity of $139\,\text{fb}^{-1}$. The helicity fractions are extracted from a fit to the normalised differential $\cos\theta^*$ distribution unfolded to parton level, in contrast to the previous ATLAS results quoted above, which measure the helicity fractions from a template fit to the detector-level distributions. This provides a complementary measurement of the fractions while also measuring the differential cross-section distribution with respect to $\cos\theta^*$.

2 The ATLAS detector

ATLAS [19–21] is a multipurpose particle detector designed with a forward–backward symmetric cylindrical geometry and nearly full 4π coverage in solid angle.[1] It consists of an inner tracking detector (ID) surrounded by a thin superconducting solenoid providing a 2 T axial magnetic field, electromagnetic and hadronic calorimeters, and a muon spectrometer (MS). The ID covers the pseudorapidity range $|\eta| < 2.5$ and is composed of silicon pixel, silicon microstrip, and transition radiation tracking detectors. Lead/liquid-argon (LAr) sampling calorimeters provide electromagnetic (EM) energy measurements with high granularity. Hadronic calorimetry is provided by the steel/scintillator-tile calorimeter covering the central pseudorapidity range ($|\eta| < 1.7$). The endcap and forward regions are instrumented with LAr calorimeters for both the EM and hadronic energy measurements up to $|\eta| = 4.9$. The MS surrounds the calorimeters and is based on three large air-core toroidal superconducting magnets with eight coils each. The field integral of the toroids ranges between 2.0 and 6.0 T m across most of the detector. The MS includes a system of precision tracking chambers and fast detectors for triggering. A two-level trigger system is used to select events. The first-level trigger is implemented in hardware and uses a subset of the detector information to keep the accepted event rate below 100 kHz [22]. This is followed by a software-based trigger that reduces the accepted event rate to 1 kHz on average. An extensive software suite [23] is used in data simulation, in the reconstruction and analysis of real and simulated data, in detector operations, and in the trigger and data acquisition systems of the experiment.

3 Data and simulated samples

This measurement exploits proton–proton collision data recorded with the ATLAS detector from 2015 to 2018 at a centre-of-mass energy of $\sqrt{s}$ = 13 TeV. After applying data-quality requirements [24], the data sample corresponds to an integrated luminosity of $139\,\text{fb}^{-1}$, determined by using the LUCID-2 detector [25] for the primary luminosity measurements. Monte Carlo (MC) simulated samples are used in the analysis to optimise the event selection, estimate the selection efficiency and predict contributions from various background processes.

---

[1] ATLAS uses a right-handed coordinate system with its origin at the nominal interaction point (IP) in the centre of the detector and the z-axis along the beam pipe. The x-axis points from the IP to the centre of the LHC ring, and the y-axis points upwards. Cylindrical coordinates (r, ϕ) are used in the transverse plane, ϕ being the azimuthal angle around the z-axis. The pseudorapidity is defined in terms of the polar angle θ as $\eta = -\ln\tan(\theta/2)$. Angular distance is measured in units of $\Delta R \equiv \sqrt{(\Delta\eta)^2 + (\Delta\phi)^2}$.

The production of $t\bar{t}$ events was modelled by the Powheg Box v2 [26–29] generator, using a next-to-leading-order (NLO) matrix element (ME), a dynamic scale [30], and an h_{damp} parameter value of $1.5m_{\mathrm{top}}$ [31].[2] The top-quark decay was modelled by a leading-order (LO) ME in Powheg Box v2, with an approximate implementation of finite-width and interference effects in Pythia 8.230 [32]. The $t\bar{t}$ sample is normalised to the cross-section prediction at NNLO in QCD, including the resummation of next-to-next-to-leading logarithmic (NNLL) soft-gluon terms calculated using Top++ 2.0 [33–39]. This cross-section corresponds to $\sigma(t\bar{t})_{\mathrm{NNLO+NNLL}} = 832 \pm 51$ pb when using a top-quark mass of $m_{\mathrm{top}} = 172.5$ GeV. Production of a top quark in association with a W boson (tW) was modelled by Powheg Box v2 at NLO in QCD using the five-flavour scheme. The diagram removal scheme [40] was used to remove interference and overlap with $t\bar{t}$ production. The inclusive cross-section is corrected to the theory prediction calculated at NLO in QCD with NNLL soft-gluon corrections [41, 42].

The production of V + jets ($V = Z, W$) events was simulated with the Sherpa 2.2.1 [43] generator, using a NLO ME for up to two partons, and a LO ME for up to four partons, calculated with the Comix [44] and OpenLoops [45–47] libraries. They were matched with the Sherpa parton shower [48] using the MEPS@NLO prescription [49–52]. The samples are normalised to a NNLO prediction [53]. Samples of diboson final states (VV) were simulated with Sherpa, including off-shell effects and Higgs boson contributions where appropriate. Fully leptonic final states and semileptonic final states, where one boson decays leptonically and the other hadronically, were generated using MEs at NLO accuracy in QCD for up to one additional parton and at LO accuracy for up to three additional parton emissions. The matrix-element calculations were matched and merged with the Sherpa parton shower based on Catani–Seymour dipole factorisation [44, 48] using the MEPS@NLO prescription. The virtual QCD corrections were provided by the OpenLoops library.

The production of $t\bar{t}V$ and $t\bar{t}H$ events was modelled at NLO using the MadGraph5_aMC@NLO 2.3.3 [54] and Powheg Box v2 generators, respectively. The simulated $t\bar{t}V$ and $t\bar{t}H$ events are normalised to the cross-sections computed at NLO in QCD with the leading NLO electroweak corrections [55–57].

For all samples of simulated events, except those generated using Sherpa, the decays of bottom and charm hadrons were performed by EvtGen [58]. In all processes, m_{top} was set to 172.5 GeV. The Powheg Box and MadGraph5_aMC@NLO generators used the NNPDF3.0nlo set of parton distribution functions (PDFs) [59] and the events were interfaced to Pythia [32] to model the parton shower, hadronisation, and underlying event, with parameter values set according to the A14 tune [60]. For events generated with Sherpa, the NNPDF3.0nnlo set of PDFs and a dedicated set of tuned parton-shower parameters were used. After the event generation, the ATLAS detector response was simulated [61] using either a full detector simulation based on Geant4 [62] or a faster parametric simulation [63] for the MC samples used to estimate the modelling uncertainties. The effect of multiple interactions in the same or neighbouring bunch-crossings (pile-up) was modelled by overlaying each hard-scattering event with simulated inelastic pp events generated by Pythia 8.186 [64] using the NNPDF2.3lo set of PDFs [65] and parameter values set according to the A3 tune [66].

The contribution from events with misreconstructed or non-prompt leptons passing the selection is estimated using MC samples for processes with one prompt lepton in the matrix element. These include single-lepton $t\bar{t}$,

---

[2] The h_{damp} parameter is a resummation damping factor and one of the parameters that controls the matching of Powheg matrix elements to the parton shower and thus effectively regulates the high-p_{T} radiation against which the $t\bar{t}$ system recoils.

$t\bar{t}V$, $t\bar{t}H$, t- and s-channel single top quark, and W + jets production. After event selection, this background contribution is less than 1% of the total predicted SM yield, including the $t\bar{t}$ events.

4 Object and event selection

Electron candidates are reconstructed from clusters of energy deposited in the electromagnetic calorimeter matched to particle tracks inside the ID. The candidates are identified with the *TightLH* likelihood-based identification criteria [67, 68]. They are required to have $p_T > 25$ GeV and $|\eta| < 2.47$, excluding the transition region $1.37 < |\eta| < 1.52$ between the barrel and endcaps. Electron candidates must also have a transverse impact-parameter significance $|d_0/\sigma(d_0)| < 5$, measured relative to the beam line, and satisfy $|z_0 \sin\theta| < 0.5$ mm, where θ is the polar angle of the track and z_0 is the longitudinal distance from the primary vertex to the point where d_0 is measured. Muon candidates are reconstructed from tracks in the MS matched to tracks in the ID. The candidates are identified with the *Medium* identification criteria [69] with $p_T > 25$ GeV and $|\eta| < 2.5$. Additionally, muon candidates must satisfy $|z_0 \sin\theta| < 0.5$ mm and $|d_0/\sigma(d_0)| < 3$. Isolated electrons and muons are selected by requiring both the amount of energy deposited close by in the calorimeters and the scalar sum of the transverse momenta of nearby tracks in the ID to be small.

Jet candidates are reconstructed from particle-flow objects [70], using the anti-k_t [71] jet algorithm with radius parameter $R = 0.4$ implemented in the FastJet [72] software. A jet energy scale calibration derived from 13 TeV data and simulation [73] is applied to the reconstructed jets. After the calibration, jet candidates are required to have $p_T > 25$ GeV and $|\eta| < 2.5$. To suppress jets originating from pile-up collisions, a 'jet vertex tagger' (JVT) [74] discriminant requirement is applied to jets with p_T below 60 GeV.

Jets containing b-hadrons are identified (b-tagged) using the DL1r algorithm [75, 76]. The algorithm combines inputs from the impact parameters of displaced vertices, as well as topological properties of secondary and tertiary vertices within a jet. These inputs are then passed to a neural network that outputs three values, representing the probability of the jet being a light-flavour jet, a c-jet or a b-jet, which are then combined into a single discriminant. The b-tagged jets are required to satisfy the operating point corresponding to 60% efficiency for identifying b-quark jets in simulated $t\bar{t}$ events.

The missing transverse momentum vector $\vec{p}_T^{\text{miss}}$, with magnitude E_T^{miss}, is defined as the negative sum of the transverse momenta of the reconstructed and calibrated physical objects, as well as a 'soft term' built from all other tracks that are associated with the primary vertex [77].

To avoid double-counting of detector signatures, overlapping physics objects are removed in the following order: electrons sharing a track with a muon; the closest jet within $\Delta R = 0.2$ of an electron; electrons within $\Delta R = 0.4$ of a jet; jets within $\Delta R = 0.4$ of a muon if they have at most two associated tracks; muons within $\Delta R = 0.4$ of a jet.[3]

Scale factors (SFs) are used to correct the efficiencies in simulation to those measured in data for the electron and muon trigger, reconstruction, identification, and isolation criteria [68, 69, 78, 79]. Additionally, the energies of the electrons [68] and the p_T of the muons [80] and jets [81, 82] are corrected using resonance

---

[3] For the overlap removal, ΔR is defined as $\Delta R \equiv \sqrt{(\Delta y)^2 + (\Delta\phi)^2}$, where $y = (1/2)[(E + p_z)/(E - p_z)]$ is the rapidity of the object.

decays. SFs are also applied for the JVT requirement [83] and for the b-tagging efficiencies for jets that originate from the hadronisation of b-quarks [75], c-quarks [84], and (u, d, s)-quarks or gluons [85]. The amount of the pile-up in simulation is corrected to reproduce the number of reconstructed primary vertices in data.

Events that satisfy the requirements of at least one of the single-electron or single-muon triggers [22, 78, 79] are selected. The events are also required to have at least one reconstructed collision vertex with two or more associated tracks with transverse momentum, p_T, greater than 500 MeV. The vertex with the highest $\sum p_T^2$ of the associated tracks is taken as the primary vertex. The selected events are required to have exactly two leptons (electrons or muons) of opposite electric charge with $p_T > 25$ GeV or $p_T > 27$ GeV for the 2015 and 2016–2018 data-taking periods, respectively, to match the increasing minimum p_T thresholds of the single-electron and single-muon triggers. One of the reconstructed charged leptons must be matched to the lepton that passed the trigger requirement. Additionally, the events are required to have at least two reconstructed jets with $p_T > 25$ GeV, with at least two of these b-tagged at the 60%-efficiency operating point. This 'tight' operating point is chosen because it reduces the background to a minimum level while keeping a large number of $t\bar{t}$ events. Furthermore, in same-flavour lepton events (e^+e^- and $\mu^+\mu^-$) the invariant mass of the two charged leptons, $m_{\ell\ell}$, is required to be outside of the Z-boson mass window of 80–100 GeV, and $E_T^{miss} > 60$ GeV is required in order to suppress background originating from Z + jets events. Finally, all events are required to have $m_{\ell\ell} > 15$ GeV to suppress low-mass resonances. After the event selection, the sample is expected to contain about 250 000 $t\bar{t}$ events. The background represents about 3.5% of all events passing the selection, with the largest contribution coming from the single-top tW process. Figure 1 compares the data with the predictions for the leading-lepton p_T distribution and the $\cos\theta^*$ distribution after the event selection.
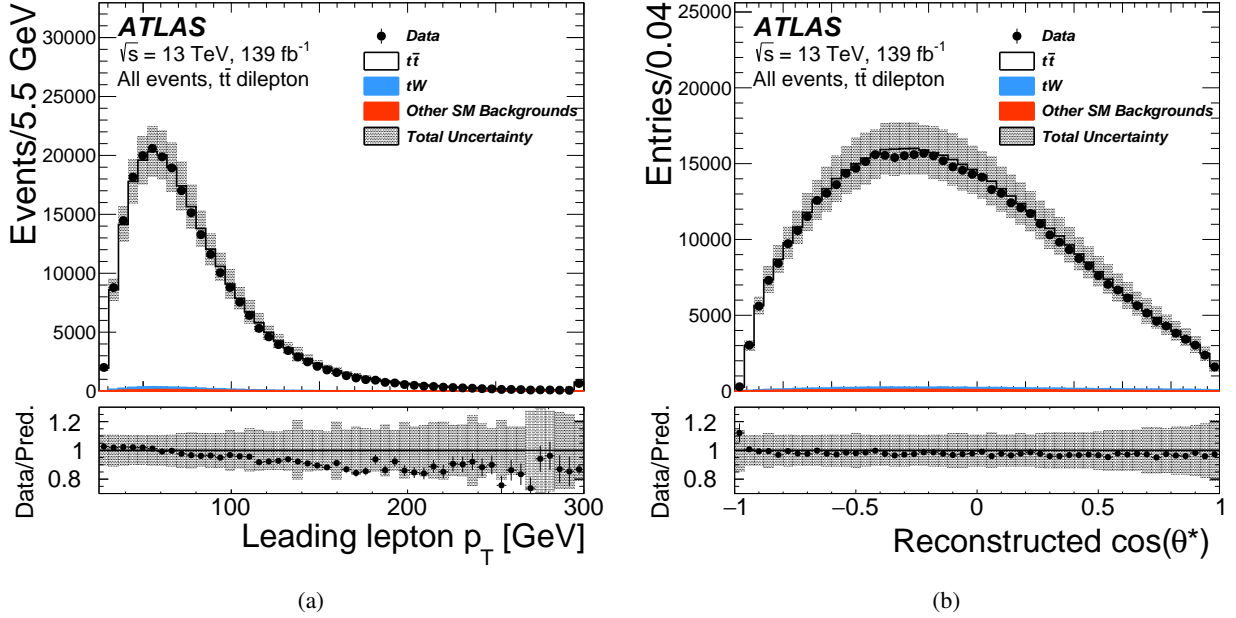
Figure 1: Comparison of observed data and predictions for (a) the p_T distribution of the leading lepton and (b) the reconstructed $\cos\theta^*$ distribution containing measurements from both hemispheres of the $t\bar{t}$ system. All three lepton-flavour channels, e^+e^-, $\mu^+\mu^-$ and $e\mu$, are combined. The hashed band represents the total uncertainty. The bottom panel shows the ratio of data to prediction. The rightmost bins contain the overflow events.

5 Reconstruction of the top-quark kinematics

The observable sensitive to the W boson helicity fractions, $\cos\theta^*$, requires reconstruction of the kinematics of the $t\bar{t}$ event from the identified leptons, jets and missing transverse momentum. The individual four-momenta of the two neutrinos from the $t\bar{t}$ dileptonic decay are not measured in the detector but the sum of their transverse momenta, E_T^{miss}, is measured and is used to reconstruct the top quark and top antiquark using the 'neutrino weighting' (NW) method [86]. The method allows the underconstrained system to be reconstructed by using the W-boson and top-quark mass constraints and scanning over the neutrino pseudorapidities to find two possible solutions for each of the assumed values of the neutrino pseudorapidities. The corresponding E_T^{miss} value is then compared with the measured E_T^{miss} of the event, and an event weight based on the degree of their agreement, which takes into account the resolution of the measured E_T^{miss}, is computed. For some events, no solution can be found, due to the finite resolution of the detector or mismeasurement of the input objects' transverse momenta. To mitigate this effect, the transverse momenta of the measured jets are varied using a Gaussian function with a p_T-dependent width between 8% and 14% of the measured jet p_T. This variation is repeated five times, increasing the probability of finding a solution. For the events with more than two b-tagged jets, the two b-jets with the highest p_T are used in the kinematic reconstruction. The top quark and top antiquark are reconstructed by assigning to their decays the b-jets and neutrino momenta corresponding to the solution with the highest weight in the NW method. A solution is found for about 90% of the $t\bar{t}$ events. Events where the NW method fails to find a solution are discarded and not used further. The reconstruction

efficiency for the background is lower, which helps to suppress it.

The statistical correlation of the distributions of $\cos\theta^*$ originating from the top quark and top antiquark was checked in the simulation and found to be small. Thus, these two $\cos\theta^*$ distributions are combined into a single distribution used in the measurement. Furthermore, since uncertainties related to lepton reconstruction are expected to be subdominant, the $\cos\theta^*$ distributions from the three lepton-flavour channels, e^+e^-, $\mu^+\mu^-$ and $e\mu$, are also combined into a single distribution, mitigating statistical fluctuations. Further investigation has shown that the increased sensitivity to systematic uncertainties, due to the different selection criteria imposed on the same-flavour channels, is not significant.

6 Differential cross-section

In order to extract W boson helicity fractions, the differential $\cos\theta^*$ cross-section is measured at parton level. The parton level is defined as the full phase-space of the dileptonically decaying W bosons from the $t\bar{t}$ decay, including τ-leptons. The leptons are taken from the MC generator's 'truth' record before final-state photon radiation, and in the case of τ-leptons, also before decay. The expected background, estimated using the MC simulation, is subtracted from the detector-level $\cos\theta^*$ distribution. The background-subtracted detector-level $\cos\theta^*$ distribution is corrected for detector effects using an iterative Bayesian unfolding (IBU) method [87] incorporated in the RooUnfold [88] package with updated corrections to the error propagation [89]. At MC-truth level, both top quarks in a $t\bar{t}$ event are required to decay leptonically.

The differential cross-section is calculated as

$$\frac{\mathrm{d}\sigma_{t\bar{t}}}{\mathrm{d}\cos\theta_i^*} = \frac{1}{\mathcal{L} \cdot \Delta X_i \cdot \epsilon_i^{\mathrm{sel}}} \cdot \sum_j R_{ij}^{-1} \cdot (N_j^{\mathrm{obs}} - N_j^{\mathrm{bkg}})$$

where i denotes a bin of the $\cos\theta^*$ distribution, ΔX_i is the width of bin i, $\mathcal{L}$ is the integrated luminosity, and N_j^{obs} and N_j^{bkg} are the observed number of data events and the estimated number of background events in bin j, respectively. The $\epsilon_i^{\mathrm{sel}}$ term corresponds to the probability for a MC-truth event to satisfy the reconstruction and selection criteria. The migration matrix R_{ij}^{-1} maps the binned parton-level events to the binned detector-level events and is derived from simulated $t\bar{t}$ events decaying into dilepton final states, following the procedure described in Ref. [90]. The probability of correct measurement of $\cos\theta^*$ is represented by the diagonal elements of the migration matrix, whereas the off-diagonal elements represent the probability of event migration between those bins.

The impact of the considered systematic uncertainties in the $\cos\theta^*$ distribution, described in Section 8, is estimated using pseudo-data obtained by systematically varying the detector-level distributions predicted by the simulation. Each varied distribution is then unfolded, and the difference between the MC-truth distribution and the unfolded distribution is considered an uncertainty in the unfolded distribution. Different sources of systematic uncertainty are uncorrelated with each other, but each is correlated across the bins.

The binning of the $\cos\theta^*$ distribution is optimised to mitigate statistical fluctuations. It is chosen such that each bin of the detector-level $\cos\theta^*$ distribution contains at least 1.5% of the total number of events and,

furthermore, at least 30% of each bin's events originate from the corresponding MC-truth bin. This procedure results in the migration matrix and selection efficiency shown in Figure 2.

MC simulated events are used to validate the unfolding method and the extraction of the W boson helicity fractions. However, it was found that the MC-truth $\cos\theta^*$ distribution deviates slightly from the quadratic formula in Eq. (1) after the simulation of the parton shower. The formula is followed exactly at the matrix-element level, but the four-momentum-reshuffling in the parton shower generator distorts the distribution at a few per mille level. To circumvent this problem and construct MC samples with well-defined true helicity fractions, the MC-truth $\cos\theta^*$ distribution is reweighted to match the functional form of Eq. (1) when using the values of the helicity fractions calculated at NNLO in QCD [3]. The weights are derived from a ratio of the MC-truth $\cos\theta^*$ distribution with a thousand bins and the analytic function in Eq. (1) with fractions set to the NNLO prediction.

Stress tests to validate the unfolding method are performed using simulated $\cos\theta^*$ distributions representing pure helicity states. These distributions are obtained for each fraction, using the reweighting procedure described in Ref. [13] to obtain $\cos\theta^*$ distributions corresponding to different values of the helicity fractions. Several stressed distributions are constructed with values of helicity fractions in ranges of f_L and f_R corresponding to 2σ variations of the measured fractions in Ref. [13]. The stressed distributions are unfolded and compared with a similarly stressed parton-level distribution to check the linearity and for potential biases. The latter are minimised by optimising the IBU regularisation parameter that controls the number of iterations in the unfolding algorithm. The optimal value is found to be 180, for which the observed bias is of the order of the expected statistical uncertainty of the measurement. This rather large regularisation parameter is due to the combination of migration matrix having large off-diagonal elements and a non-linear $\cos\theta^*$ distribution.
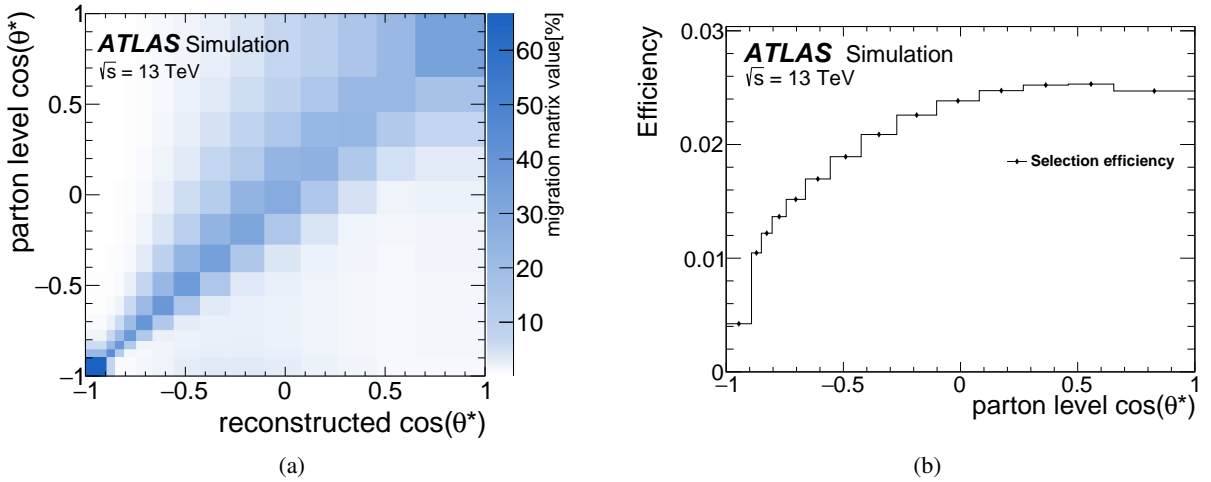

(a)

(b)

Figure 2: Migration matrix (Figure 2(a)) and selection efficiency per bin (Figure 2(b)). The migration matrix is obtained as a result of the bin optimisation. The entries represent probabilities (expressed as percentages) for an event with $\cos\theta^*$ in bin i at parton level to have reconstructed $\cos\theta^*$ in bin j at detector level. The selection efficiency is calculated with respect to the true $t\bar{t}$ dilepton events in the bin. The error bars on the selection efficiency points are too small to be seen in the distribution.

7 Extraction of the helicity fractions

The helicity fractions are extracted by fitting Eq. (1) to the measured normalised differential cross-section distribution and minimising the χ^2 defined as

$$\chi^2 = \Delta y^{\mathrm{T}} C^{-1} \Delta y, \tag{2}$$

where Δy is a vector containing the differences between the bin yield in data and the value of the function in Eq. (1). Due to the unitarity constraint on the sum of the helicity fractions, the parameter representing one of the fractions is replaced with one minus the sum of the other helicity fractions.

For each bin, the function is evaluated at the point along the horizontal axis where the expected bin yield matches the value of the function defined by Eq. (1). This choice is motivated by the non-linear shape of the analytic function. The matrix C is the covariance matrix of the normalised differential cross-section distribution and contains both the statistical and systematic uncertainties. The covariance matrix is generated according to the procedure described in Ref. [90]. Statistical and systematic uncertainties are estimated using 'toy' experiments on the pre-unfolded detector-level $\cos\theta^*$ distribution in data and then propagating the variations to the unfolded distribution. The statistical uncertainty is estimated by applying independent Poisson fluctuations to the individual bins. Systematic uncertainties are estimated using Gaussian smearing of individual bins by the corresponding systematic variation. All of these changes to the distribution are summed in quadrature to estimate the total uncertainty per bin.

Since a normalised distribution is used in the fit, one degree of freedom is removed by removing one bin of the $\cos\theta^*$ distribution from Eq. (2). The minimisation is carried out using the MINUIT program [91]. The parameters representing the helicity fractions are not restricted in the fit, and are allowed to take unphysical values outside of the [0, 1] interval.

Linearity tests of the helicity fraction extraction procedure are performed with stressed distributions generated as described in Section 6. For each stressed distribution, the χ^2 defined by Eq. (2) is minimised with the covariance matrix computed when including only the MC statistical uncertainty, and the extracted values of the helicity fractions are compared with their input values. Any non-closure seen is included as a systematic uncertainty of the measurement.

8 Systematic uncertainties

Systematic uncertainties may affect the selection efficiency for the $t\bar{t}$ signal, the bin migrations, the number of events expected from the background processes, and the shapes of the background distributions. These effects are estimated by varying each source of systematic uncertainty by one standard deviation and considering the resulting deviation from the nominal expectation as the uncertainty. For the extraction of the helicity fractions, the systematic uncertainties enter the covariance matrix that is used in the fit as described in Section 7.

The effects of uncertainties in the modelling of the $t\bar{t}$ signal are estimated by independently varying the renormalisation and factorisation scales in the matrix element by factors of 0.5 and 2, but normalising the

signal to the nominal cross-section. A variation of the Var3c parameter of the A14 tune [92], which impacts the renormalisation scale for initial-state radiation, is considered independently. An uncertainty from the final-state radiation modelling is estimated by doubling and halving the nominal renormalisation scale for emissions from the parton shower. Additionally, an uncertainty due to the choice of parton shower generator is estimated by comparing the nominal MC sample with an alternative MC sample that uses Herwig 7.1.3 [93, 94] with the H7UE set of tuned parameters [94] and the MMHT2014lo PDF set [95] instead of the Pythia 8.230 generator. Furthermore, an uncertainty due to the nominal choice of generator is estimated by comparing the nominal prediction with the prediction from MadGraph5_aMC@NLO 2.6.0 [54] interfaced with Herwig 7.1.3. The uncertainty due to the choice of the h_{damp} parameter value is estimated by increasing its value by a factor of two and symmetrising the impact. The uncertainty due to using a top-quark mass of 172.5 GeV is estimated by raising and lowering the mass by 0.5 GeV, which is approximately the uncertainty in the measurement of the top-quark mass by the ATLAS Collaboration [96]. The PDF uncertainty is estimated by considering the internal variations of the PDF4LHC [97] PDF set. For all $t\bar{t}$ modelling uncertainties, all predictions are reweighted to match the NNLO helicity fractions in the full phase-space as described in Section 6.

For the tW process, effects of uncertainties in the renormalisation and factorisation scales, the Var3c parameter value in the A14 tune, and final-state radiation modelling are estimated following the same procedure as used for the $t\bar{t}$ signal. Additionally, an uncertainty due to the nominal choice of parton shower and hadronisation generator is estimated by comparing the nominal MC prediction with a prediction using Herwig 7.0.4 instead of the Pythia 8.230 generator. An uncertainty due to the choice of generator is estimated by comparing distributions from MadGraph5_aMC@NLO 2.6.0 with the nominal ones from Powheg Box v2. Furthermore, an uncertainty due to the overlap between the tW and $t\bar{t}$ processes is estimated by comparing samples using the diagram removal scheme with those using the diagram subtraction scheme [40].

An uncertainty of 5.3%, estimated from the scale and PDF variations [41], is applied to the tW background normalisation. A conservative 50% cross-section uncertainty is used for $t\bar{t}V$, $t\bar{t}H$, $Z+$jets, and VV production and for processes with non-prompt leptons. This conservative uncertainty was found to have negligible impact on the final result.

An uncertainty of 1.7% in the integrated luminosity is considered for all processes [98]. The uncertainty due to pile-up is determined by varying the average number of interactions per bunch-crossing by 3% in the simulation. Uncertainties in the calibration, reconstruction and identification of the different reconstructed objects are also considered. For electrons and muons, these include the uncertainties in the measured SFs for triggering, reconstruction, identification and isolation [68, 69, 78, 79], as well as in the electron- and muon-momentum calibration and resolution [68, 80]. For hadronic jets, the uncertainties in the jet energy scale (JES) [81] and jet energy resolution (JER) [82], as well as the uncertainties in the SFs for the JVT [83] and the tagging of jets as b-jets [75, 84, 85], are considered. All uncertainties associated with reconstructed objects are propagated to the $E_{\mathrm{T}}^{\mathrm{miss}}$ and an uncertainty in the soft term is also considered [77]. The JES and JER uncertainties are determined using a model with 30 and 8 independent components, respectively. The uncertainties in the b-tagging calibration include nine/five/five independent variations for the b-/c-/light-jet calibrations and two components for the MC-based uncertainty extrapolation to very high p_{T} jets.

9 Results

Figure 3(a) shows unfolded $\cos\theta^*$ differential distribution with statistical and total uncertainties compared with the prediction of $t\bar{t}$ MC simulation. The unfolded normalised $\cos\theta^*$ distribution along with the fit function used to measure the helicity fractions f_0, f_L and f_R is shown in Figure 3(b). In the fit, f_L and f_R are free parameters and the f_0 parameter is set to $f_0 = 1 - f_L - f_R$ to preserve the unitarity of the sum of the three parameters. The helicity fractions are found to be

$$f_0 = 0.684 \pm 0.005 \text{ (stat.)} \pm 0.014 \text{ (syst.)},$$
$$f_L = 0.318 \pm 0.003 \text{ (stat.)} \pm 0.008 \text{ (syst.)},$$
$$f_R = -0.002 \pm 0.002 \text{ (stat.)} \pm 0.014 \text{ (syst.)},$$

with the covariance and correlation matrices of the fit shown in Table 1. The χ^2 divided by the number of degrees of freedom of the fit is 0.267, demonstrating good agreement between the fitted functional form and data corrected to parton level. The covariance matrix is estimated from a 2×2 matrix obtained directly from the fit, with a third row and column calculated analytically from the unitarity constraint on the helicity fractions. The obtained values and uncertainties, including the covariance matrix, do not change if any two of the parameters are chosen as free parameters and the third one is calculated analytically.

The expected uncertainties in the helicity fraction obtained from a fit to the MC predictions are identical to the measured uncertainties.

As a further test of the unfolding procedure, a $\cos\theta^*$ distribution is generated in the Monte Carlo, based on the measured values of the helicity fractions; this distribution is unfolded, helicity fractions are extracted, and compared to the input values. A small degree of non-closure is observed but the corresponding uncertainty is negligible and does not change the total uncertainties listed in Table 2.

Table 1: Covariance matrix and correlation matrix for the measured helicity fractions.

	Covariance			Correlation		
	f_0	f_L	f_R	f_0	f_L	f_R
f_0	2.125×10^{-4}	-3.665×10^{-5}	-1.758×10^{-4}	1	-0.308	-0.841
f_L	-3.665×10^{-5}	6.651×10^{-5}	-2.986×10^{-5}	-0.308	1	-0.255
f_R	-1.758×10^{-4}	-2.986×10^{-5}	2.057×10^{-4}	-0.841	-0.255	1

The impact of different categories of systematic uncertainty and the data's statistical uncertainty on the f_0, f_L and f_R measurement is summarised in Table 2. They are estimated by generating a covariance matrix which includes all sources of uncertainty except for the considered category and repeating the fit. The considered category contributes an uncertainty whose square is the difference of the squares of nominal-fit and repeated-fit symmetrised total uncertainties for each helicity fraction. The systematic uncertainty dominates
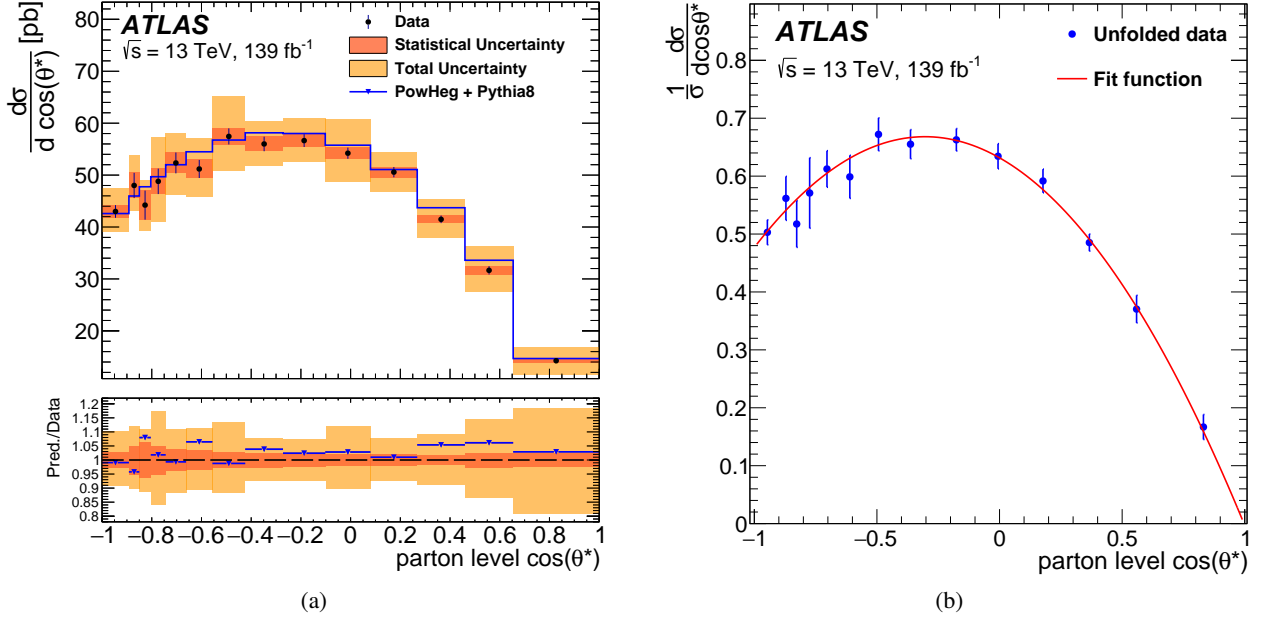
Figure 3: The unfolded $\cos\theta^*$ differential distribution (Figure 3(a)) and the unfolded normalised $\cos\theta^*$ distribution (Figure 3(b)). The total statistical and systematic uncertainty per bin is shown in Figure 3(a). The parton-level distribution predicted by POWHEG BOX interfaced with PYTHIA is shown. An uncertainty originating from the limited number of simulated events is included in the prediction but is not visible. The unfolded normalised $\cos\theta^*$ distribution in data is shown with the function of Eq. (1) overlaid, using the helicity fractions f_0, f_L and f_R determined from the fit. The total uncertainties are shown on data points.

the total uncertainty for all three helicity fractions. The largest systematic uncertainty in all three helicity fractions arises from the modelling of $t\bar{t}$ production, and is dominated by the uncertainty from the choice of matrix-element generator. Other significant uncertainties come from the jet energy scale and resolution as well as electron and muon reconstruction.

The impact on the extracted helicity fractions arising from the mis-modeling of the top-quark p_T distribution in the MC simulation was tested by correcting the top-quark p_T in simulation to match the calculation at NNLO in QCD with NLO electroweak corrections [99]. No significant effect on the expected uncertainty was observed.

Table 2: Impact of different categories of systematic uncertainty and the data's statistical uncertainty on the f_0, f_L and f_R measurement. The squares of the quoted numbers are evaluated as the difference of the squares of the nominal-fit total uncertainties (quoted in the last row) and those extracted from a fit using a covariance matrix including all sources of uncertainty except for the considered category. In the latter fits with partial covariance matrices, the best-fit values for the helicity fractions are shifted by up to a quarter of the uncertainty found by the fit with the full covariance matrix. The total uncertainty is different from the sum in quadrature of the different components because of correlations between different uncertainties entering the covariance matrix.

Category	σ_{f_0}	σ_{f_L}	σ_{f_R}
Detector modelling			
Jet reconstruction	0.008	0.004	0.010
Flavour tagging	0.003	0.001	0.001
Electron reconstruction	0.003	0.002	0.002
Muon reconstruction	0.003	0.003	$< 10^{-3}$
E_T^{miss} (soft term)	$< 10^{-3}$	0.002	$< 10^{-3}$
Pile-up	0.002	0.002	$< 10^{-3}$
Luminosity	0.001	0.001	$< 10^{-3}$
Signal and background modelling			
$t\bar{t}$ production	0.011	0.005	0.010
PDF	0.002	0.001	$< 10^{-3}$
Single top production	$< 10^{-3}$	0.002	$< 10^{-3}$
Other background	0.002	0.001	$< 10^{-3}$
Total systematic uncertainty	0.014	0.008	0.014
Data statistical uncertainty	0.005	0.003	0.002
Total uncertainty	0.015	0.008	0.014

10 Conclusion

A measurement of the W boson helicity fractions using $t\bar{t}$ events in the dilepton final state is presented. It used data from 13 TeV pp collisions collected by the ATLAS detector at the LHC, corresponding to an integrated luminosity of 139 fb^{-1}. The fractions are extracted from the normalised differential cross-section distribution of $\cos \theta^*$ corrected to the parton level. This provides a complementary measurement of the helicity fractions to the previously published ATLAS results. The measured fractions of longitudinal, left- and right-handed polarisation states are found to be $f_0 = 0.684 \pm 0.005$ (stat.) ± 0.014 (syst.), $f_L = 0.318 \pm 0.003$ (stat.) ± 0.008 (syst.) and $f_R = -0.002 \pm 0.002$ (stat.) ± 0.014 (syst.), in agreement within one standard deviation with the Standard Model calculation at NNLO in QCD.

References

[1] CDF Collaboration, *Observation of top quark production in $\bar{p}p$ collisions*,
Phys. Rev. Lett. **74** (1995) 2626, arXiv: `hep-ex/9503002 [hep-ex]`.

[2] D0 Collaboration, *Observation of the top quark*, Phys. Rev. Lett. **74** (1995) 2632,
arXiv: `hep-ex/9503003 [hep-ex]`.

[3] A. Czarnecki, J. G. Körner and J. H. Piclum,
Helicity fractions of W bosons from top quark decays at next-to-next-to-leading order in QCD,
Phys. Rev. D **81** (2010) 111503, arXiv: `1005.2625 [hep-ph]`.

[4] J. A. Aguilar-Saavedra, *A minimal set of top anomalous couplings*, Nucl. Phys. B **812** (2009) 181,
arXiv: `0811.3842 [hep-ph]`.

[5] C. Zhang and S. Willenbrock, *Effective-field-theory approach to top-quark production and decay*,
Phys. Rev. D **83** (2011) 034006, arXiv: `1008.3869 [hep-ph]`.

[6] I. Brivio et al., *O new physics, where art thou? A global search in the top sector*, JHEP **02** (2020) 131,
arXiv: `1910.03606 [hep-ph]`.

[7] ALEPH Collaboration,
Measurement of W-pair production in e^+e^- collisions at centre-of-mass energies from 183 to 209 GeV,
Eur. Phys. J. C **38** (2004) 147.

[8] DELPHI Collaboration, *Measurement of the W-pair production cross-section and W branching ratios
in e^+e^- collisions at $\sqrt{s}$ = 161-209 GeV*, Eur. Phys. J. C **34** (2004) 127.

[9] L3 Collaboration, *Measurement of the cross section of W-boson pair production at LEP*,
Phys. Lett. B **600** (2004) 22, arXiv: `hep-ex/0409016`.

[10] OPAL Collaboration,
W^+W^- production cross-section and W branching fractions in e^+e^- collisions at 189 GeV,
Phys. Lett. B **493** (2000) 249, arXiv: `hep-ex/0009019`.

[11] The ALEPH, DELPHI, L3, OPAL Collaborations, the LEP Electroweak Working Group,
Electroweak Measurements in Electron-Positron Collisions at W-Boson-Pair Energies at LEP,
Phys. Rept. **532** (2013) 119, arXiv: `1302.3415 [hep-ex]`.

[12] J. A. Aguilar-Saavedra and J. Bernabeu,
Breaking down the entire W boson spin observables from its decay, Phys. Rev. D **93** (2016) 011301,
arXiv: `1508.04592 [hep-ph]`.

[13] ATLAS Collaboration, *Measurement of the W boson polarisation in $t\bar{t}$ events from pp collisions at
$\sqrt{s}$ = 8 TeV in the lepton+jets channel with ATLAS*, Eur. Phys. J. C **77** (2017) 264,
arXiv: `1612.02577 [hep-ex]`, Erratum: Eur. Phys. J. C **79** (2019) 19.

[14] CMS Collaboration, *Measurement of the W boson helicity fractions in the decays of top quark pairs to
lepton+jets final states produced in pp collisions at $\sqrt{s}$ = 8 TeV*, Phys. Lett. B **762** (2016) 512,
arXiv: `1605.09047 [hep-ex]`.

[15] CDF Collaboration,
Measurement of W-Boson Polarization in Top-quark Decay in $p\bar{p}$ Collisions at sqrt(s) = 1.96 TeV,
Phys. Rev. Lett. **105** (2010) 042002, arXiv: `1003.0224 [hep-ex]`.

[16] D0 Collaboration,
Measurement of the W boson helicity in top quark decays using 5.4 fb^{-1} of $p\bar{p}$ collision data,
Phys. Rev. D **83** (2011) 032009, arXiv: 1011.6549 [hep-ex].

[17] CDF and D0 Collaboration,
Combination of CDF and D0 measurements of the W boson helicity in top quark decays,
Phys. Rev. D **85** (2012) 071106, arXiv: 1202.5272 [hep-ex].

[18] ATLAS and CMS Collaborations, *Combination of the W boson polarization measurements in top quark decays using ATLAS and CMS data at $\sqrt{s}$ = 8 TeV*, JHEP **08** (2020) 051,
arXiv: 2005.03799 [hep-ex].

[19] ATLAS Collaboration, *The ATLAS Experiment at the CERN Large Hadron Collider*,
JINST **3** (2008) S08003.

[20] B. Abbott et al., *Production and integration of the ATLAS Insertable B-Layer*,
JINST **13** (2018) T05008, arXiv: 1803.00844 [physics.ins-det].

[21] ATLAS Collaboration, *ATLAS Insertable B-Layer Technical Design Report Addendum*,
CERN-LHCC-2012-009, Addendum to CERN-LHCC-2010-013, ATLAS-TDR-019, 2012,
URL: https://cds.cern.ch/record/1451888.

[22] ATLAS Collaboration, *Performance of the ATLAS trigger system in 2015*,
Eur. Phys. J. C **77** (2017) 317, arXiv: 1611.09661 [hep-ex].

[23] ATLAS Collaboration, *The ATLAS Collaboration Software and Firmware*, ATL-SOFT-PUB-2021-001,
2021, URL: https://cds.cern.ch/record/2767187.

[24] ATLAS Collaboration, *ATLAS data quality operations and performance for 2015–2018 data-taking*,
JINST **15** (2020) P04003, arXiv: 1911.04632 [physics.ins-det].

[25] G. Avoni et al., *The new LUCID-2 detector for luminosity measurement and monitoring in ATLAS*,
JINST **13** (2018) P07017.

[26] S. Frixione, G. Ridolfi and P. Nason,
A positive-weight next-to-leading-order Monte Carlo for heavy flavour hadroproduction,
JHEP **09** (2007) 126, arXiv: 0707.3088 [hep-ph].

[27] P. Nason, *A new method for combining NLO QCD with shower Monte Carlo algorithms*,
JHEP **11** (2004) 040, arXiv: hep-ph/0409146.

[28] S. Frixione, P. Nason and C. Oleari,
Matching NLO QCD computations with parton shower simulations: the POWHEG method,
JHEP **11** (2007) 070, arXiv: 0709.2092 [hep-ph].

[29] S. Alioli, P. Nason, C. Oleari and E. Re, *A general framework for implementing NLO calculations in shower Monte Carlo programs: the POWHEG BOX*, JHEP **06** (2010) 043,
arXiv: 1002.2581 [hep-ph].

[30] ATLAS Collaboration, *Comparison of Monte Carlo generator predictions from Powheg and Sherpa to ATLAS measurements of top pair production at 7 TeV*, ATL-PHYS-PUB-2015-011, 2015,
URL: https://cds.cern.ch/record/2020602.

[31] ATLAS Collaboration, *Studies on top-quark Monte Carlo modelling for Top2016*,
ATL-PHYS-PUB-2016-020, 2016, URL: https://cds.cern.ch/record/2216168.

[32] T. Sjöstrand et al., *An introduction to PYTHIA 8.2*, Comput. Phys. Commun. **191** (2015) 159,
arXiv: 1410.3012 [hep-ph].

[33] M. Beneke, P. Falgari, S. Klein and C. Schwinn,
Hadronic top-quark pair production with NNLL threshold resummation, Nucl. Phys. B **855** (2012) 695,
arXiv: 1109.1536 [hep-ph].

[34] M. Cacciari, M. Czakon, M. Mangano, A. Mitov and P. Nason, *Top-pair production at hadron colliders
with next-to-next-to-leading logarithmic soft-gluon resummation*, Phys. Lett. B **710** (2012) 612,
arXiv: 1111.5869 [hep-ph].

[35] P. Bärnreuther, M. Czakon and A. Mitov, *Percent-Level-Precision Physics at the Tevatron:
Next-to-Next-to-Leading Order QCD Corrections to $q\bar{q} \to t\bar{t} + X$*, Phys. Rev. Lett. **109** (2012) 132001,
arXiv: 1204.5201 [hep-ph].

[36] M. Czakon and A. Mitov,
NNLO corrections to top-pair production at hadron colliders: the all-fermionic scattering channels,
JHEP **12** (2012) 054, arXiv: 1207.0236 [hep-ph].

[37] M. Czakon and A. Mitov,
NNLO corrections to top pair production at hadron colliders: the quark-gluon reaction,
JHEP **01** (2013) 080, arXiv: 1210.6832 [hep-ph].

[38] M. Czakon, P. Fiedler and A. Mitov,
Total Top-Quark Pair-Production Cross Section at Hadron Colliders Through $O(\alpha_S^4)$,
Phys. Rev. Lett. **110** (2013) 252004, arXiv: 1303.6254 [hep-ph].

[39] M. Czakon and A. Mitov,
Top++: A program for the calculation of the top-pair cross-section at hadron colliders,
Comput. Phys. Commun. **185** (2014) 2930, arXiv: 1112.5675 [hep-ph].

[40] S. Frixione, E. Laenen, P. Motylinski, C. White and B. R. Webber,
Single-top hadroproduction in association with a W boson, JHEP **07** (2008) 029,
arXiv: 0805.3067 [hep-ph].

[41] N. Kidonakis,
Two-loop soft anomalous dimensions for single top quark associated production with a W^- or H^-,
Phys. Rev. D **82** (2010) 054018, arXiv: 1005.4451 [hep-ph].

[42] N. Kidonakis, 'Top Quark Production', *Proceedings, Helmholtz International Summer School on
Physics of Heavy Quarks and Hadrons (HQ 2013)* (JINR, Dubna, Russia, 15th–28th July 2013) 139,
arXiv: 1311.0283 [hep-ph].

[43] E. Bothmann et al., *Event generation with Sherpa 2.2*, SciPost Phys. **7** (2019) 034,
arXiv: 1905.09127 [hep-ph].

[44] T. Gleisberg and S. Höche, *Comix, a new matrix element generator*, JHEP **12** (2008) 039,
arXiv: 0808.3674 [hep-ph].

[45] F. Buccioni et al., *OpenLoops 2*, Eur. Phys. J. C **79** (2019) 866, arXiv: 1907.13071 [hep-ph].

[46] F. Cascioli, P. Maierhöfer and S. Pozzorini, *Scattering Amplitudes with Open Loops*, Phys. Rev. Lett. **108** (2012) 111601, arXiv: `1111.5206 [hep-ph]`.

[47] A. Denner, S. Dittmaier and L. Hofer, *Collier: A fortran-based complex one-loop library in extended regularizations*, Comput. Phys. Commun. **212** (2017) 220, arXiv: `1604.06792 [hep-ph]`.

[48] S. Schumann and F. Krauss, *A parton shower algorithm based on Catani–Seymour dipole factorisation*, JHEP **03** (2008) 038, arXiv: `0709.1027 [hep-ph]`.

[49] S. Höche, F. Krauss, M. Schönherr and F. Siegert, *A critical appraisal of NLO+PS matching methods*, JHEP **09** (2012) 049, arXiv: `1111.1220 [hep-ph]`.

[50] S. Höche, F. Krauss, M. Schönherr and F. Siegert, *QCD matrix elements + parton showers. The NLO case*, JHEP **04** (2013) 027, arXiv: `1207.5030 [hep-ph]`.

[51] S. Catani, F. Krauss, B. R. Webber and R. Kuhn, *QCD Matrix Elements + Parton Showers*, JHEP **11** (2001) 063, arXiv: `hep-ph/0109231`.

[52] S. Höche, F. Krauss, S. Schumann and F. Siegert, *QCD matrix elements and truncated showers*, JHEP **05** (2009) 053, arXiv: `0903.1219 [hep-ph]`.

[53] C. Anastasiou, L. Dixon, K. Melnikov and F. Petriello, *High-precision QCD at hadron colliders: Electroweak gauge boson rapidity distributions at next-to-next-to leading order*, Phys. Rev. D **69** (2004) 094008, arXiv: `hep-ph/0312266`.

[54] J. Alwall et al., *The automated computation of tree-level and next-to-leading order differential cross sections, and their matching to parton shower simulations*, JHEP **07** (2014) 079, arXiv: `1405.0301 [hep-ph]`.

[55] J. M. Campbell and R. K. Ellis, *$t\bar{t}W^{\pm}$ production and decay at NLO*, JHEP **07** (2012) 052, arXiv: `1204.5678 [hep-ph]`.

[56] S. Frixione, V. Hirschi, D. Pagani, H.-S. Shao and M. Zaro, *Electroweak and QCD corrections to top-pair hadroproduction in association with heavy bosons*, JHEP **06** (2015) 184, arXiv: `1504.03446 [hep-ph]`.

[57] D. de Florian et al., *Handbook of LHC Higgs Cross Sections: 4. Deciphering the Nature of the Higgs Sector*, (2016), arXiv: `1610.07922 [hep-ph]`.

[58] D. J. Lange, *The EvtGen particle decay simulation package*, Nucl. Instrum. Meth. A **462** (2001) 152.

[59] R. D. Ball et al., *Parton distributions for the LHC run II*, JHEP **04** (2015) 040, arXiv: `1410.8849 [hep-ph]`.

[60] ATLAS Collaboration, *ATLAS Pythia 8 tunes to 7 TeV data*, ATL-PHYS-PUB-2014-021, 2014, URL: `https://cds.cern.ch/record/1966419`.

[61] ATLAS Collaboration, *The ATLAS Simulation Infrastructure*, Eur. Phys. J. C **70** (2010) 823, arXiv: `1005.4568 [physics.ins-det]`.

[62] GEANT4 Collaboration, S. Agostinelli et al., *Geant4 – a simulation toolkit*, Nucl. Instrum. Meth. A **506** (2003) 250.

18

[63] ATLAS Collaboration,
The simulation principle and performance of the ATLAS fast calorimeter simulation FastCaloSim,
ATL-PHYS-PUB-2010-013, 2010, URL: https://cds.cern.ch/record/1300517.

[64] T. Sjöstrand, S. Mrenna and P. Skands, *A brief introduction to PYTHIA 8.1*,
Comput. Phys. Commun. **178** (2008) 852, arXiv: 0710.3820 [hep-ph].

[65] R. D. Ball et al., *Parton distributions with LHC data*, Nucl. Phys. B **867** (2013) 244,
arXiv: 1207.1303 [hep-ph].

[66] ATLAS Collaboration, *The Pythia 8 A3 tune description of ATLAS minimum bias and inelastic
measurements incorporating the Donnachie–Landshoff diffractive model*, ATL-PHYS-PUB-2016-017,
2016, URL: https://cds.cern.ch/record/2206965.

[67] ATLAS Collaboration, *Electron and photon reconstruction and performance in ATLAS using a
dynamical, topological cell clustering-based approach*, ATL-PHYS-PUB-2017-022, 2017,
URL: https://cds.cern.ch/record/2298955.

[68] ATLAS Collaboration, *Electron and photon performance measurements with the ATLAS detector using
the 2015–2017 LHC proton–proton collision data*, JINST **14** (2019) P12006,
arXiv: 1908.00005 [hep-ex].

[69] ATLAS Collaboration, *Muon reconstruction and identification efficiency in ATLAS using the full Run 2
pp collision data set at $\sqrt{s} = 13$ TeV*, Eur. Phys. J. C **81** (2021) 578, arXiv: 2012.00578 [hep-ex].

[70] ATLAS Collaboration,
Jet reconstruction and performance using particle flow with the ATLAS Detector,
Eur. Phys. J. C **77** (2017) 466, arXiv: 1703.10485 [hep-ex].

[71] M. Cacciari, G. P. Salam and G. Soyez, *The anti-k_t jet clustering algorithm*, JHEP **04** (2008) 063,
arXiv: 0802.1189 [hep-ph].

[72] M. Cacciari, G. P. Salam and G. Soyez, *FastJet user manual*, Eur. Phys. J. C **72** (2012) 1896,
arXiv: 1111.6097 [hep-ph].

[73] ATLAS Collaboration, *Jet energy scale and resolution measured in proton–proton collisions at
$\sqrt{s} = 13$ TeV with the ATLAS detector*, Eur. Phys. J. C **81** (2020) 689, arXiv: 2007.02645 [hep-ex].

[74] ATLAS Collaboration, *Performance of pile-up mitigation techniques for jets in pp collisions at
$\sqrt{s} = 8$ TeV using the ATLAS detector*, Eur. Phys. J. C **76** (2016) 581, arXiv: 1510.03823 [hep-ex].

[75] ATLAS Collaboration, *ATLAS b-jet identification performance and efficiency measurement with $t\bar{t}$
events in pp collisions at $\sqrt{s} = 13$ TeV*, Eur. Phys. J. C **79** (2019) 970, arXiv: 1907.05120 [hep-ex].

[76] ATLAS Collaboration,
Optimisation and performance studies of the ATLAS b-tagging algorithms for the 2017-18 LHC run,
ATL-PHYS-PUB-2017-013, 2017, URL: https://cds.cern.ch/record/2273281.

[77] ATLAS Collaboration, *Performance of missing transverse momentum reconstruction with the ATLAS
detector using proton–proton collisions at $\sqrt{s} = 13$ TeV*, Eur. Phys. J. C **78** (2018) 903,
arXiv: 1802.08168 [hep-ex].

[78] ATLAS Collaboration, *Performance of electron and photon triggers in ATLAS during LHC Run 2*,
Eur. Phys. J. C **80** (2020) 47, arXiv: 1909.00761 [hep-ex].

[79] ATLAS Collaboration, *Performance of the ATLAS muon triggers in Run 2*, JINST **15** (2020) P09015, arXiv: 2004.13447 [hep-ex].

[80] ATLAS Collaboration, *Muon reconstruction performance of the ATLAS detector in proton–proton collision data at $\sqrt{s} = 13$ TeV*, Eur. Phys. J. C **76** (2016) 292, arXiv: 1603.05598 [hep-ex].

[81] ATLAS Collaboration, *Jet energy scale measurements and their systematic uncertainties in proton–proton collisions at $\sqrt{s} = 13$ TeV with the ATLAS detector*, Phys. Rev. D **96** (2017) 072002, arXiv: 1703.09665 [hep-ex].

[82] ATLAS Collaboration, *Jet Calibration and Systematic Uncertainties for Jets Reconstructed in the ATLAS Detector at $\sqrt{s} = 13$ TeV*, ATL-PHYS-PUB-2015-015, 2015, URL: https://cds.cern.ch/record/2037613.

[83] ATLAS Collaboration, *Tagging and suppression of pileup jets with the ATLAS detector*, ATLAS-CONF-2014-018, 2014, URL: https://cds.cern.ch/record/1700870.

[84] ATLAS Collaboration, *Measurement of the c-jet mistagging efficiency in $t\bar{t}$ events using pp collision data at $\sqrt{s} = 13$ TeV collected with the ATLAS detector*, Eur. Phys. J. C **82** (2021) 95, arXiv: 2109.10627 [hep-ex].

[85] ATLAS Collaboration, *Calibration of light-flavour b-jet mistagging rates using ATLAS proton–proton collision data at $\sqrt{s} = 13$ TeV*, ATLAS-CONF-2018-006, 2018, URL: https://cds.cern.ch/record/2314418.

[86] D0 Collaboration, *Measurement of the Top Quark Mass Using Dilepton Events*, Phys. Rev. Lett. **80** (1998) 2063, arXiv: hep-ex/9706014 [hep-ex].

[87] G. D'Agostini, *A multidimensional unfolding method based on Bayes' theorem*, Nucl. Instrum. Meth. A **362** (1995) 487.

[88] T. Adye, 'Unfolding algorithms and tests using RooUnfold', *Proceedings, 2011 Workshop on Statistical Issues Related to Discovery Claims in Search Experiments and Unfolding (PHYSTAT 2011)* (CERN, Geneva, Switzerland, 17th–20th Jan. 2011) 313, arXiv: 1105.1160 [physics.data-an].

[89] H. B. Prosper and L. Lyons, eds., *Proceedings, PHYSTAT 2011 Workshop on Statistical Issues Related to Discovery Claims in Search Experiments and Unfolding, CERN,Geneva, Switzerland 17-20 January 2011*, CERN, Geneva: CERN, 2011, ISBN: 9789290833673, URL: https://doi.org/10.5170/CERN-2011-006.

[90] ATLAS Collaboration, *Measurements of top-quark pair single- and double-differential cross-sections in the all-hadronic channel in pp collisions at $\sqrt{s} = 13$ TeV using the ATLAS detector*, JHEP **01** (2021) 033, arXiv: 2006.09274 [hep-ex].

[91] F. James and M. Roos, *Minuit: A System for Function Minimization and Analysis of the Parameter Errors and Correlations*, Comput. Phys. Commun **10** (1975) 343.

[92] ATLAS Collaboration, *Studies on top-quark Monte Carlo modelling with Sherpa and MG5_aMC@NLO*, ATL-PHYS-PUB-2017-007, 2017, URL: https://cds.cern.ch/record/2261938.

[93] M. Bähr et al., *Herwig++ physics and manual*, Eur. Phys. J. C **58** (2008) 639,
arXiv: 0803.0883 [hep-ph].

[94] J. Bellm et al., *Herwig 7.0/Herwig++ 3.0 release note*, Eur. Phys. J. C **76** (2016) 196,
arXiv: 1512.01178 [hep-ph].

[95] L. A. Harland-Lang, A. D. Martin, P. Motylinski and R. S. Thorne,
Parton distributions in the LHC era: MMHT 2014 PDFs, Eur. Phys. J. C **75** (2015) 204,
arXiv: 1412.3989 [hep-ph].

[96] ATLAS Collaboration, *Measurement of the top quark mass in the $t\bar{t} \rightarrow$ lepton+jets and
$t\bar{t} \rightarrow$ dilepton channels using $\sqrt{s} = 7$ TeV ATLAS data*, Eur. Phys. J. C **75** (2015) 330,
arXiv: 1503.05427 [hep-ex].

[97] J. Butterworth et al., *PDF4LHC recommendations for LHC Run II*, J. Phys. G **43** (2016) 023001,
arXiv: 1510.03865 [hep-ph].

[98] ATLAS Collaboration,
Luminosity determination in pp collisions at $\sqrt{s} = 13$ TeV using the ATLAS detector at the LHC,
ATLAS-CONF-2019-021, 2019, URL: https://cds.cern.ch/record/2677054.

[99] M. Czakon et al., *Top-pair production at the LHC through NNLO QCD and NLO EW*,
JHEP **10** (2017) 186, arXiv: 1705.04105 [hep-ph].